

RhythmMamba: Fast Remote Physiological Measurement with Arbitrary Length Videos

Bochao Zou

University of Science and Technology Beijing
Beijing, China
zoubochao@ustb.edu.cn

Xiaocheng Hu

China Academy of Electronics and Information
Technology
Beijing, China
675342900@qq.com

Zizheng Guo

University of Science and Technology Beijing
Beijing, China
guozizheng@xs.ustb.edu.cn

Huimin Ma*

University of Science and Technology Beijing
Beijing, China
mhmpub@ustb.edu.cn

ABSTRACT

Remote photoplethysmography (rPPG) is a non-contact method for detecting physiological signals from facial videos, holding great potential in various applications such as healthcare, affective computing, and anti-spoofing. Existing deep learning methods struggle to address two core issues of rPPG simultaneously: extracting weak rPPG signals from video segments with large spatiotemporal redundancy and understanding the periodic patterns of rPPG among long contexts. This represents a trade-off between computational complexity and the ability to capture long-range dependencies, posing a challenge for rPPG that is suitable for deployment on mobile devices. Based on the in-depth exploration of Mamba's comprehension of spatial and temporal information, this paper introduces RhythmMamba, an end-to-end Mamba-based method that employs multi-temporal Mamba to constrain both periodic patterns and short-term trends, coupled with frequency domain feed-forward to enable Mamba to robustly understand the quasi-periodic patterns of rPPG. Extensive experiments show that RhythmMamba achieves state-of-the-art performance with reduced parameters and lower computational complexity. The proposed RhythmMamba can be applied to video segments of any length without performance degradation. The codes are available at <https://github.com/zizheng-guo/RhythmMamba>.

CCS CONCEPTS

• **Computing methodologies** → **Biometrics**.

KEYWORDS

rPPG, Video Understanding, Video Mamba, Arbitrary Length Videos

1 INTRODUCTION

Blood Volume Pulse (BVP) is an important physiological signal, further allowing for the extraction of key vital signs such as heart rate (HR) and heart rate variability (HRV). Photoplethysmography (PPG) is a non-invasive monitoring method that utilizes optical means to measure changes in blood volume within living tissues. The physiological mechanism underlying BVP extraction from PPG is rooted in variations in light absorption and scattering due to changes in blood volume during cardiac contraction and relaxation

in subcutaneous blood vessels. These variations result in periodic color signal alterations on imaging sensors, imperceptible to the human eye [4, 51]. Traditionally, BVP extraction required the use of contact sensors, introducing inconveniences and limitations. In recent years, non-contact methods for extracting BVP information, specifically remote photoplethysmography (rPPG), have garnered increasing attention [5, 11, 17, 23, 33, 34]. These methods hold the promise not only to transform ubiquitous cameras into accurate health sensors for healthcare applications but also exhibit extensive application prospects and research value in various domains such as affective computing and deepfake detection, especially given the widespread dissemination of generated content in the current landscape of social media videos.

Early research on rPPG primarily relied on traditional signal processing methods to analyze facial videos and extract their periodic signals. However, rPPG signals are so weak that noise from environmental light, motion, etc., may introduce significant artifacts. Solely relying on signal processing methods often struggles to achieve satisfactory accuracy in complex environments. In recent years, data-driven methods, represented by convolutional neural networks and transformers, have become mainstream. However, convolutional neural networks have limited receptive fields and transformer-based architectures exhibit mediocre performance in capturing long-term dependencies from the computational complexity perspective, especially when dealing with long video sequences.

Recently, Mamba [13] has emerged with its selective state space model (SSM), striking a balance between maintaining linear complexity and facilitating long-term dependency modeling. It has been successfully applied to various artificial intelligence tasks such as video understanding [3, 24, 54]. For rPPG tasks that typically require long-term monitoring and are suitable for deployment on mobile devices, the linear complexity and ability to capture long-term dependencies give Mamba an advantage. However, capturing weak rPPG signals accurately amidst numerous spatiotemporal token sequences remains a challenge due to their susceptibility to noise from light, motion, etc.

Motivated by the aforementioned discussion, we propose a fully end-to-end model, RhythmMamba, for remote physiological measurement. By learning from the same sequences with varying temporal scales, a single Mamba block can simultaneously be constrained by the periodicity of long sequences and the trends of

*Corresponding author.

short sequences. Subsequently, through frequency domain feed-forward, the learned feature maps by Mamba undergo inter-channel interaction in the frequency domain, enabling a better discernment of periodic properties in rPPG signals.

Furthermore, through comprehensive experiments, we find that spatial information within token sequences, even with temporal embedding, somewhat interferes with Mamba’s understanding of temporal sequences. To mitigate this, we integrate rPPG information from single frame into channel information for a token using the frame stem module, boosting Mamba’s learning. Additionally, due to linear complexity of Mamba and frame global average pooling, the computational cost of RhythmMamba grows linearly with video length. Benefit from this advantage, we explore its performance under different temporal lengths and find that the proposed RhythmMamba comprehensively understands the periodic patterns of rPPG and can effectively adapt to videos of any length.

The main contributions are as follows:

- We propose RhythmMamba, which leverages state space models to robustly understand the quasi-periodic patterns of rPPG by multi-temporal Mamba learning and frequency domain feed-forward channel interacting. To the best of our knowledge, it is the first work to investigate state space models in rPPG tasks.
- In response to the observed phenomenon where spatial information interferes with Mamba’s understanding of temporal sequences, we designed the frame stem module to aggregate spatial information into channels to boost Mamba’s learning.
- Benefit from the advantage of RhythmMamba’s low computational cost for long temporal sequences, we explore the performance of RhythmMamba under long-time series inputs, demonstrating RhythmMamba’s ability to seamlessly migrate to video segments of arbitrary lengths without performance degradation.
- We conduct extensive experiments on both intra-dataset and cross-dataset scenarios. The results demonstrate that our approach achieves state-of-the-art performance with reduced parameters and lower computational complexity.

2 RELATED WORK

2.1 Remote Physiological Estimation

Previous research on rPPG predominantly relied on traditional signal processing methods to analyze facial videos for extracting their periodic signals [8, 9, 22, 25, 40, 41, 51–53]. With the advancement of deep learning, an increasing number of data-driven approaches have emerged, showcasing a trend in backbones transitioning from 2D CNNs [4, 6, 27, 36–38, 46] to 3D CNNs [21, 23, 49, 58, 59, 63] and further to transformer [15, 18, 26, 28, 42, 43, 57, 60–62, 65]. However, none of them have been able to effectively address the two core issues of rPPG: extracting weak rPPG signals from video segments with large spatiotemporal redundancy and understanding the periodic patterns of rPPG among long contexts. This represents a trade-off between complexity and the ability to capture long-range dependencies, posing a challenge for rPPG that is suitable for deployment on mobile devices. Although previously dominant 3D convolutional neural networks and video transformers have effectively tackled one of the above issues by utilizing local convolutions or long-range attention, they fail to address both problems simultaneously.

2.2 Mamba

To address the bottleneck of long sequence modeling, the state space model has received extensive research attention. It can be viewed as a hybrid of recurrent neural networks (RNNs) and convolutional neural networks (CNNs). Among these studies, a representative work is the structured state space model (S4) [14] and its variants [12, 35, 44]. Recently, Mamba has distinguished itself with a data-dependent SSM layer and a selection mechanism utilizing parallel scanning, striking a balance between maintaining linear complexity and facilitating long-term dependency modeling. Compared to transformers with quadratic complexity attention [1, 50], Mamba excels at handling long sequences with linear complexity. Subsequently, the immense potential of Mamba has sparked a series of works [3, 24, 30, 39, 54, 64] demonstrating superior performance and higher GPU efficiency of Mamba over Transformers on visual downstream tasks. However, unlike most video tasks, facial rPPG measurement requires understanding the periodic patterns of rPPG from subtle skin color variations, which may pose a challenge for conventional Mamba architecture due to its susceptibility to noise from light, motion, etc.

3 METHODOLOGY

Section 3.1 introduces the general framework of RhythmMamba, followed by the presentation of its main components: the frame stem in Section 3.2, the multi-temporal Mamba in Section 3.3, and lastly, the frequency domain feed-forward in Section 3.4.

3.1 The general framework of RhythmMamba

Compared to non-end-to-end methods that require complex preprocessing procedures [11, 32, 43], RhythmMamba is a fully end-to-end approach that takes raw video as input and produces rPPG signals as output. As shown in Figure 1, RhythmMamba consists of frame stem, multi-temporal Mamba, frequency domain feed-forward, and rPPG prediction head. The frame stem utilizes diff-fusion, self-attention, and frame average pooling to extract rPPG features and consolidate all spatial information into token channels. Specifically, given an RGB video input $X \in \mathbb{R}^{3 \times T \times H \times W}$, $X_{stem} = frame_stem(X)$, where $X_{stem} \in \mathbb{R}^{T/2 \times C}$, and C, T, W, H indicate channel, sequence length, width, and height, respectively.

Subsequently, the output of the frame stem will be fed into the multi-temporal Mamba. The tokens will be sliced into sequences of varying temporal lengths, followed by the processing of hidden information between tokens with the state space model. Then, the output of Mamba will be passed into the frequency domain feed-forward, facilitating the interaction of information across multiple channels. The outputs of Mamba and FFN will undergo normalization and residual connections. The two outputs will have dimensions identical to the output of the frame stem $X_{stem} \in \mathbb{R}^{T/2 \times C}$. Finally, the rPPG features will be upsampled and projected into BVP waves through a prediction head.

3.2 Frame Stem

In the field of video understanding, existing transformer-based and Mamba-based methods typically segment spatiotemporal information into token sequences through patch embedding [1, 3, 10, 54, 64]. Previous works on rPPG have also been based on such foundational

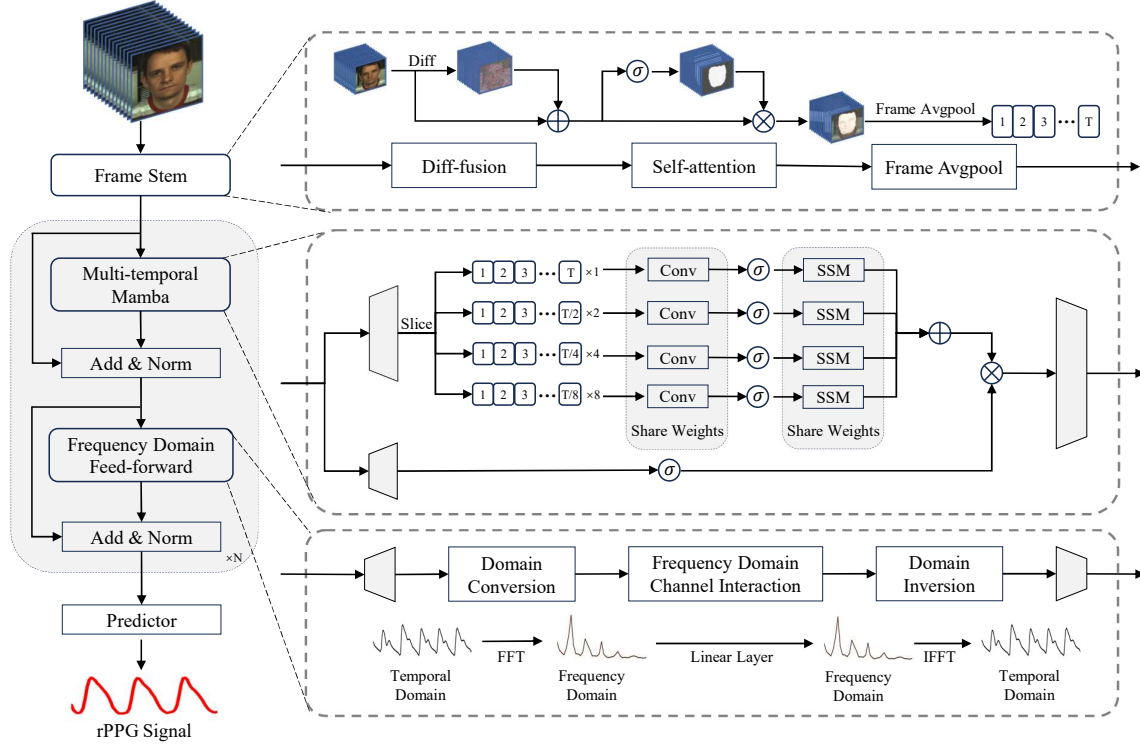


Figure 1: The framework of RhythmMamba. It consists of frame stem, multi-temporal Mamba, frequency domain feed-forward, and rPPG predictor head. Here, "+" represents addition, "×" represents multiplication, " σ " represents the activation layer, and trapezoid represents the linear layer.

models for improvements. For transformer-based methods, spatiotemporal sequences can inspire long-range spatiotemporal attention both within frames and across frames. However, we found that for linear Mamba, spatial sequences tend to interfere with Mamba’s understanding of temporal information [See section 4.5]. The frame stem is utilized to initially extract rPPG features, incorporating spatial information fully into the channels, thereby boosting the subsequent learning of temporal information in the multi-temporal Mamba and the interaction between channels in the frequency domain feed-forward.

Firstly, the diff-fusion module integrates frame difference into the raw frame, enabling frame-level representation awareness of BVP wave variations. This effectively enhances the features of rPPG with minimal additional computational cost. Additionally, for rPPG, high-frequency information across frames and low-frequency information within frames are required. Therefore, large convolutional kernels are used to obtain low-frequency information within frames, ensuring that spatial information is fully incorporated into the channels.

Specifically, for an input video $X \in \mathbb{R}^{3 \times T \times H \times W}$, temporal shift is applied to obtain $X_{t-2}, X_{t-1}, X_t, X_{t+1}$ and X_{t+2} . Then, the differences between consecutive frames are computed in chronological order, resulting in D_{-2}, D_{-1}, D_1 and D_2 . These frame differences, along with the raw frames, are passed through $Stem_1$ for primary feature extraction. $Stem_1$ consists of a 2D convolution with the kernel size of (7×7) , cascaded by batch normalization (BN), ReLU, and

MaxPool. The input dimension is 3 when taking the single-frame feature as the input, and 12 when taking the concatenation of frame differences as the input.

$$\begin{aligned} X_{diff} &= Stem_1(Concat(D_{-2}, D_{-1}, D_1, D_2)), \\ X_{origin} &= Stem_1(X_t). \end{aligned} \quad (1)$$

Then the features of the difference video and the raw video are merged and the feature representation is further enhanced through $Stem_2$, which also consists of a 2D convolution with the kernel size of (7×7) , cascaded by BN and ReLU.

$$X_{fusion} = \alpha \cdot Stem_2(X_{origin}) + \beta \cdot Stem_2(\alpha \cdot X_{origin} + \beta \cdot X_{diff}). \quad (2)$$

The fusion coefficients α and β are both set to 0.5 experimentally. The output of the diff-fusion is a fused and strengthened feature representation.

Subsequently, at the resolution of (16×16) , $Stem_3$ utilizes a (5×5) relatively large kernel convolution to fully integrate spatial information into the channels. Before frame-level global average pooling, to effectively capture rich information, a self-attention module is employed to enhance skin regions with stronger signals in the spatial domain. This self-attention module utilizes sigmoid activation followed by L1 normalization, which is softer than softmax and generates fewer masks. There is no additional 2D convolution in self-attention. In fact, the $Stem_3$ can also be regarded as a part of

the attention mechanism. The attention mask can be computed as:

$$Mask = \frac{(H/8)(W/8) \cdot \sigma(Stem_3(X_{fusion}))}{2\|\sigma(Stem_3(X_{fusion}))\|_1}. \quad (3)$$

Finally, the attention output, denoted as $X_{attn} \in \mathbb{R}^{C \times T/2 \times H/8 \times W/8}$, undergoes global average pooling within each frame, resulting in the stem output $X_{stem} \in \mathbb{R}^{T/2 \times C}$.

3.3 Multi-temporal Mamba

Past studies [7, 16, 19] have demonstrated the effectiveness of modeling periodic tasks with multi scales, mainly by extracting temporal information from paths of different scales. Unlike prior research, our approach is fundamentally distinct in two aspects: 1. The method is different. We slice a video segment into numerous subsegments of varying lengths to constrain a single Mamba block, rather than downsampling the video segment to different resolutions and using multiple Mamba blocks to extract information jointly; 2. The motivation differs as well. We aim to subject a Mamba block to both the periodic constraints of long sequences and the trend constraints of short sequences simultaneously, rather than extracting different features from multi-temporal scales.

As shown in Figure 1, after the input is fed into the multi-temporal Mamba, it is linearly projected and then sliced into time sequences of different lengths. These sequences are then passed through a Mamba block and sequentially go through convolutional layers, activation layers, and state space models. The state space model is a type of linear time-invariant system that maps inputs to outputs through hidden layers. SSM is typically modeled by the following ordinary differential equations:

$$\begin{aligned} h'(t) &= Ah(t) + Bx(t), \\ y(t) &= Ch(t). \end{aligned} \quad (4)$$

Where $A \in \mathbb{R}^{N \times N}$ is the evolution matrix, $B \in \mathbb{R}^{N \times 1}$ and $C \in \mathbb{R}^{1 \times N}$ are the projection matrices. N represents the sequence length. This continuous system is challenging to apply, while the SSM in Mamba serves as its discrete counterpart. It discretizes continuous parameters A and B into their discrete counterparts \bar{A} and \bar{B} using a time-scale parameter Δ . This transformation typically employs the zero-order hold method:

$$\begin{aligned} \bar{A} &= \exp(\Delta A), \\ \bar{B} &= (\Delta A)^{-1}(\exp(\Delta A) - I)\Delta B, \\ h_t &= \bar{A}h_{t-1} + \bar{B}x_t, \\ y_t &= Ch_t. \end{aligned} \quad (5)$$

The practical application of this discretization form is hindered by its inherent sequential nature. Nevertheless, it can be effectively represented through a convolution operation:

$$\begin{aligned} \bar{K} &= (C\bar{B}, C\bar{A}\bar{B}, \dots, C\bar{A}^{N-1}\bar{B}), \\ y &= x * \bar{K}. \end{aligned} \quad (6)$$

Where $\bar{K} \in \mathbb{R}^N$ denotes a structured convolution kernel, and $*$ indicates a convolution operation.

3.4 Frequency Domain Feed-forward

The feed-forward network (FFN) employs linear transformations to map data into a higher-dimensional space before projecting it back into a lower-dimensional space. Through this channel interaction, deeper features are extracted. Previous works in rPPG have sometimes introduced a depthwise 3D convolution layer between the two linear layers of vanilla FFN to refine parts of noisy features and provide relative positional cues [60, 61]. In our study, due to the input sequences being solely time-dependent and the periodic nature of rPPG, channel interaction in the frequency domain enables a better discernment of the periodic properties in rPPG signals. The frequency with the strongest power within the rPPG frequency band can be interpreted as the heart rate.

The frequency domain feed-forward introduces a frequency domain linear layer between the two linear layers of vanilla FFN. The architecture of the frequency domain linear layer consists of three stages: domain conversion, frequency domain channel interaction, and domain inversion. Domain conversion and inversion utilize fast Fourier transform and inverse Fourier transform, respectively. The utilization of the Fourier transform enables the decomposition of rPPG signals into their constituent frequencies, facilitating the recognition of periodic patterns in the rPPG signal. Frequency domain channel interaction is performed through linear layer, the theoretical feasibility of which has been demonstrated by [55].

Domain Conversion/Inversion. We transform the input $H(t)$ to the frequency domain $H(f)$ as follows:

$$\begin{aligned} H(f) &= \int_{-\infty}^{\infty} H(t)e^{-j2\pi ft} dt \\ &= \int_{-\infty}^{\infty} H(t) \cos(2\pi ft) dt + j \int_{-\infty}^{\infty} H(t) \sin(2\pi ft) dt \\ &= H(f)_{re} + jH(f)_{im}. \end{aligned} \quad (7)$$

Where f represents frequency, t represents temporal, and the subscripts re and im denote the real and imaginary components of the corresponding complex data, respectively. After channel interaction in the frequency domain, inverse Fourier transform can be employed to revert to the temporal domain:

$$\begin{aligned} H(t) &= \int_{-\infty}^{\infty} H(f)e^{j2\pi ft} df \\ &= \int_{-\infty}^{\infty} (H(f)_{re} + jH(f)_{im})e^{j2\pi ft} df. \end{aligned} \quad (8)$$

Frequency Domain Channel Interaction. With the aid of the frame stem, spatial information is fully integrated into the channels. Linear layer is employed to facilitate interaction across different channels, and channel dependencies are learned by sharing the same weights across timestamps. Channel interaction in the frequency domain allows for a clearer focus on heart rate and reduces noise interference. Specifically, for complex input $H \in \mathbb{R}^{T/2 \times C}$, given complex weight matrix $W \in \mathbb{R}^{C \times C}$ and complex bias $B \in \mathbb{R}^C$, according to the rules of complex multiplication, it can be expressed as:

$$\begin{aligned}
H'_{re} &= H_{re}W_{re} - H_{im}W_{im} + B_{re}, \\
H'_{im} &= H_{re}W_{im} + H_{im}W_{re} + B_{im}, \\
H' &= H'_{re} + j \cdot H'_{im}.
\end{aligned} \tag{9}$$

After inverse FFT transform, the frequency domain feed-forward outputs through linear projection, resulting in $X_{FFN} \in \mathbb{R}^{T/2 \times C}$.

4 EXPERIMENT

4.1 Dataset and performance metric

Three publicly available datasets were used for evaluation: PURE [47], UBFC-rPPG [2], and MMPD [48]. Specifically, PURE contains 60 1-minute videos comprised of 10 participants engaged in six activities, with a video resolution of 640x480 and a frame rate of 30Hz. UBFC-rPPG contains 42 videos, recording subjects in a stationary state, with a resolution of 640x480 and a frame rate of 30Hz. MMPD comprised 33 participants with Fitzpatrick skin types 3-6. These participants performed four different activities (static, head rotation, speech, and walking) under four lighting conditions (LED-high, LED-low, incandescent, natural). The dataset included 660 1-minute videos with a resolution of 320x240 and a frame rate of 30Hz. Notably, MMPD has two versions: a compressed mini-MMPD and an uncompressed MMPD. In this study, the mini-MMPD was chosen for experimentation. Clearly, among the three datasets, PURE and UBFC are relatively easy, while MMPD stands out with a significantly larger sample size and more complex environment. Five commonly used metrics: Mean Absolute Error (MAE), Root Mean Squared Error (RMSE), Mean Absolute Percentage Error (MAPE), Pearson correlation coefficient (ρ), and Signal-to-Noise Ratio (SNR) were used for evaluation.

4.2 Implementation Details

We leveraged the rPPG toolbox [29], an open-source toolbox based on PyTorch, to implement the proposed method. A comparative analysis was conducted against several state-of-the-art methods, all implemented with the same toolbox. We followed the protocol outlined in [56] by employing random upsampling, downsampling, and horizontal flipping for data augmentation. For each video segment, the facial region was cropped and resized to 128x128 pixels in the first frame, and this region was fixed in the subsequent frames. In post-processing, a second-order Butterworth filter (cutoff frequencies: 0.75 and 2.5 Hz) is applied to filter the predicted PPG waveform. The Welch algorithm is then employed to compute the power spectral density for further heart rate estimation. The learning rate was set to 3e-4. The batch size was set to 16, and the training process spanned 30 epochs. Network training was conducted on NVIDIA RTX 3090.

Loss. We utilized a loss function incorporating both temporal and frequency domain constraints. The temporal loss \mathcal{L}_{Time} is computed using the negative Pearson correlation coefficient, and the frequency loss is calculated using the cross-entropy between the predicted BVP wave’s frequency domain and the heart rate derived from the actual BVP wave. The frequency loss \mathcal{L}_{Freq} is expressed by: $\mathcal{L}_{Freq} = CE(\maxIndex(PSD(BVP_{gt})), PSD(BVP_{pred}))$, where PSD represents Power Spectral Density, and \maxIndex represents

Table 1: Intra-dataset results on PURE and UBFC.

Method	PURE			UBFC		
	MAE	RMSE	ρ	MAE	RMSE	ρ
HR-CNN[46]	1.84	2.37	0.98	4.90	5.89	0.64
DeepPhys[4]	0.83	1.54	0.99	6.27	10.82	0.65
SynRhythm[36]	2.71	4.86	0.98	5.59	6.82	0.72
PhysNet[58]	2.10	2.60	0.99	2.95	3.67	0.97
rPPGNet[59]	0.74	1.21	-	0.56	0.73	0.99
Meta-rPPG[20]	2.52	4.63	0.98	5.97	7.42	0.53
TS-CAN[27]	2.48	9.01	0.92	1.70	2.72	0.99
Siamese[49]	0.51	1.56	0.83	0.48	0.97	-
PulseGAN[45]	2.28	4.29	0.99	-	-	-
Dual-GAN[32]	0.82	1.31	0.99	0.44	0.67	0.99
AND-rPPG[31]	-	-	-	2.67	4.07	0.92
TDM[6]	1.83	2.30	0.99	2.32	3.08	0.99
PhysFormer[61]	1.10	1.75	0.99	0.50	0.71	0.99
EfficientPhys[28]	-	-	-	1.14	1.81	0.99
RADIANT[15]	-	-	-	2.91	4.52	-
Li et al.[23]	1.44	2.50	-	0.76	1.62	-
LSTC[21]	-	-	-	0.70	1.00	0.99
zhang et al.[62]	1.53	2.29	0.99	-	-	-
RhythmFormer[65]	0.27	0.47	0.99	0.50	0.78	0.99
RhythmMamba(Ours)	0.23	0.34	0.99	0.50	0.75	0.99

Table 2: Intra-dataset results on MMPD.

Method	MMPD				
	MAE	RMSE	MAPE	ρ	SNR
DeepPhys[4]	22.27	28.92	23.9	-0.03	-13.44
PhysNet[58]	4.80	11.80	4.74	0.60	1.77
TS-CAN[27]	9.71	17.22	10.36	0.44	-6.69
PhysFormer[61]	11.99	18.41	12.50	0.18	-9.51
EfficientPhys[28]	13.47	21.32	14.19	0.21	-9.25
RhythmFormer[65]	3.07	6.81	3.24	0.86	5.46
RhythmMamba(Ours)	<u>3.16</u>	<u>7.27</u>	<u>3.37</u>	<u>0.84</u>	<u>4.74</u>

the index of the maximum value. The overall loss is expressed by: $\mathcal{L}_{Overall} = \alpha \cdot \mathcal{L}_{Time} + \beta \cdot \mathcal{L}_{Freq}$.

4.3 Intra-dataset evaluation

For the evaluation of the PURE dataset, we adhered to the protocol outlined in [32, 46]. Specifically, the first 60% of the dataset was utilized for training, while the remaining 40% was allocated for testing. Similarly, for the evaluation of the UBFC dataset, we followed the protocol specified in [32, 45], selecting the initial 30 samples for training and the subsequent 12 samples for testing. As illustrated in Table 1, on the PURE dataset, our method outperformed state-of-the-art methods across all metrics. In the case of the UBFC dataset, our method demonstrated comparable performance to state-of-the-art methods.

Due to the relative simplicity of PURE and UBFC, the performance of state-of-the-art methods on these two datasets is nearing saturation. We further evaluated using the challenging MMPD

Table 3: Cross-dataset results. Best results are marked in bold and second best in underline.

Method	TrainSet	Test Set														
		PURE					UBFC					MMPD				
		MAE	RMSE	MAPE	ρ	SNR	MAE	RMSE	MAPE	ρ	SNR	MAE	RMSE	MAPE	ρ	SNR
GREEN[51]	-	10.09	23.85	10.28	0.34	-2.66	19.73	31.00	18.72	0.37	-11.18	21.68	27.69	24.39	-0.01	-14.34
ICA[41]	-	4.77	16.07	4.47	0.72	5.24	16.00	25.65	15.35	0.44	-9.91	18.60	24.30	20.88	0.01	-13.84
CHROM[8]	-	5.77	14.93	11.52	0.81	4.58	4.06	8.83	3.84	0.89	-2.96	13.66	18.76	16.00	0.08	-11.74
LGI[40]	-	4.61	15.38	4.96	0.77	4.50	15.80	28.55	14.70	0.36	-8.15	17.08	23.32	18.98	0.04	-13.15
PBV[9]	-	3.92	12.99	4.84	0.84	2.30	15.90	26.40	15.17	0.48	-9.16	17.95	23.58	20.18	0.09	-13.88
POS[52]	-	3.67	11.82	7.25	0.88	6.87	4.08	7.72	3.93	0.92	-2.39	12.36	17.71	14.43	0.18	-11.53
DeepPhys[4]	UBFC	5.54	18.51	5.32	0.66	4.40	-	-	-	-	-	17.50	25.00	19.27	0.06	-11.72
	PURE	-	-	-	-	-	1.21	2.90	1.42	0.99	1.74	16.92	24.61	18.54	0.05	-11.53
PhysNet[58]	UBFC	8.06	19.71	13.67	0.61	6.68	-	-	-	-	-	<u>9.47</u>	<u>16.01</u>	11.11	0.31	-8.15
	PURE	-	-	-	-	-	0.98	2.48	1.12	0.99	1.49	13.94	21.61	15.15	0.20	-9.94
TS-CAN[27]	UBFC	3.69	13.80	3.39	0.82	5.26	-	-	-	-	-	14.01	21.04	15.48	0.24	-10.18
	PURE	-	-	-	-	-	1.30	2.87	1.50	0.99	1.49	13.94	21.61	15.15	0.20	-9.94
PhysFormer[61]	UBFC	12.92	24.36	23.92	0.47	2.16	-	-	-	-	-	12.10	17.79	15.41	0.17	-10.53
	PURE	-	-	-	-	-	1.44	3.77	1.66	0.98	0.18	14.57	20.71	16.73	0.15	-12.15
EfficientPhys[28]	UBFC	5.47	17.04	5.40	0.71	4.09	-	-	-	-	-	13.78	22.25	15.15	0.09	-9.13
	PURE	-	-	-	-	-	2.07	6.32	2.10	0.94	-0.12	14.03	21.62	15.32	0.17	-9.95
Spiking-Phys[26]	UBFC	<u>2.70</u>	-	<u>4.93</u>	0.91	-	-	-	-	-	-	13.36	-	15.46	0.20	-
	PURE	-	-	-	-	-	5.25	-	4.96	0.83	-	12.76	-	15.59	0.23	-
RhythmFormer[65]	UBFC	0.97	3.36	1.60	0.99	12.01	-	-	-	-	-	9.08	15.07	11.17	0.53	-7.73
	PURE	-	-	-	-	-	0.89	<u>1.83</u>	0.97	0.99	<u>6.05</u>	8.98	14.85	11.11	0.51	-8.39
Ours	UBFC	2.87	<u>9.58</u>	5.31	<u>0.92</u>	<u>8.12</u>	-	-	-	-	-	10.51	17.15	12.20	<u>0.33</u>	<u>-7.89</u>
	PURE	-	-	-	-	-	<u>0.96</u>	1.78	<u>1.03</u>	0.99	6.72	<u>10.45</u>	<u>16.49</u>	<u>12.20</u>	<u>0.37</u>	<u>-8.40</u>

dataset, following the protocol of [65], partitioning it sequentially into training, validation, and test sets in a ratio of 7:1:2. As depicted in Table 2, we compared our method against existing state-of-the-art approaches. Facing the more complex environmental conditions of MMPD, our method achieved a state-of-the-art level. This demonstrates the excellent rPPG feature extraction capability of RhythmMamba and underscores its enhanced robustness.

4.4 Cross-Dataset Evaluation

In addition, we followed the protocol outlined in [29] for cross-dataset evaluation. The models were trained on PURE and UBFC individually and subsequently tested on PURE, UBFC, and MMPD datasets. The training dataset was split, with the initial 80% used for training and the remaining 20% for validation. Comparative results against state-of-the-art end-to-end methods are presented in Table 3. The results highlight the superior capability of RhythmMamba in modeling domain-invariant rPPG features and its good generalization ability across diverse datasets. RhythmMamba demonstrates the feasibility of the Mamba architecture for the rPPG task.

4.5 Ablation Study

We conducted ablation experiments on the MMPD dataset to assess the impact of different modules.

Impact of Spatial Information. We replaced the frame global average pooling of frame stem with patch embedding for comparative experiments, where both position embedding and temporal

Table 4: Impact of Spatial information (with Vanilla FFN)

Spatio Token numbers	MAE	RMSE	MAPE	ρ	SNR
8×8	4.90	10.14	5.15	0.71	-2.10
4×4	4.62	8.87	4.83	0.77	-0.88
4×4 (Temporal Embedding)	4.92	10.04	5.07	0.69	-1.43
4×4 (Position Embedding)	5.47	10.34	5.77	0.71	-3.03
2×2	4.69	9.97	4.80	0.70	-0.98
1×1 (Avgpool)	3.54	7.68	3.72	0.82	2.88

embedding were implemented utilizing learnable parameters. For a fair comparison, the comparative experiments all use vanilla FFN, as token sequences purely based on temporal may have an advantage in one-dimensional FFT. As shown in Table 4, replacing average pooling with patch embedding resulted in significant performance degradation, even with temporal embedding and position embedding. From the experimental results, it appears that spatial sequence may greatly interfere with Mamba’s understanding of the temporal sequence. For linear Mamba, it may be advantageous to distribute multidimensional information across different channels, with each channel retaining single-dimensional information.

Impact of Key Module. As illustrated in Table 5, the comparison between the first four rows and the last row indicates the significant roles played by diff-fusion, self-attention, relative large kernel, and multi-temporal. Here, "relative large kernel" refers to

Table 5: Impact of Key Module

Diff-fusion	Self-attention	Large Kernel	Multi-temporal	FFN	MAE	RMSE	MAPE	ρ	SNR
×	✓	✓	✓	Frequency	5.71	10.00	5.97	0.68	-0.29
✓	×	✓	✓	Frequency	4.02	8.43	4.15	0.79	2.98
✓	✓	×	✓	Frequency	3.51	7.53	3.81	0.83	4.22
✓	✓	✓	×	Frequency	3.60	7.78	3.83	0.81	4.38
✓	✓	✓	✓	×	3.53	7.65	3.67	0.83	2.89
✓	✓	✓	✓	Vanilla	3.54	7.68	3.72	0.82	2.88
✓	✓	✓	✓	Spatio-Temporal	3.82	8.06	3.95	0.81	4.06
✓	✓	✓	✓	Frequency	3.16	7.27	3.37	0.84	4.74

Table 6: Arbitrary length videos input

Train Length	Test Length	MAE	RMSE	MAPE	ρ	SNR
160	160	3.16	7.27	3.37	0.84	4.74
160	30(1s)	5.50	11.65	6.02	0.66	-1.70
160	80(2.6s)	3.11	6.61	3.30	0.87	3.09
160	300(10s)	3.21	7.43	3.42	0.83	6.11
160	600(20s)	3.10	7.61	3.32	0.82	8.15
160	900(30s)	3.51	7.30	3.70	0.84	8.56
160	1800(60s)	3.14	7.04	3.30	0.85	10.59
300(10s)	300(10s)	3.23	7.25	3.51	0.84	5.19
600(20s)	600(20s)	4.64	9.82	4.99	0.72	8.41
900(30s)	900(30s)	6.48	12.64	6.95	0.60	8.21
1800(60s)	1800(60s)	11.52	18.38	12.31	0.33	-1.40

the usage of a (7×7) convolution kernel when downsampling to (32×32) resolution in the stem, and a (5×5) convolution kernel when downsampling to (16×16) resolution. The ablation will replace them with the kernel of size (3×3) . The use of relatively large convolution kernels allows for the integration of spatial information into channels effectively, thereby providing sufficient information for subsequent Mamba processing.

Impact of Frequency Domain Feed-forward. As shown in Table 5, the comparison of the last four rows shows that the frequency domain FFN plays an important role. Among them, vanilla FFN refers to the two linear layers to conduct FFN, and Spatio-Temporal FFN refers to the addition of a depthwise 3D convolution layer between the linear layers [61]. Frequency domain FFN adds a frequency domain linear layer between the linear layers, effectively extracting and analyzing the most critical frequency domain features in rPPG.

4.6 Arbitrary length videos input

The computational complexity of Mamba is $O(T)$ in RhythmMamba, while the transformer’s complexity is $O((HWT)^2)$, and Mamba without average pooling is $O(HWT)$. Here, H and W represent the number of patches divided by spatial embedding, and T represents the temporal length of the sequence. A single NVIDIA RTX 3090 can support RhythmMamba inference for videos lasting over 5 minutes.

We train RhythmMamba on video segments of 160 frames and test it on videos of arbitrary lengths, with the longest test video being limited to 60 seconds due to dataset constraints. As observed

Table 7: Computational Cost.

Method	Param. (M)	MACs (G)
DeepPhys[4]	7.504	120.000
PhysNet[58]	0.700	70.120
TS-CAN[27]	7.504	120.000
PhysFormer[61]	7.381	50.607
EfficientPhys[28]	7.439	60.687
RhythmFormer[65]	3.251	38.494
RhythmMamba(Ours)	1.065	12.943

in the first 7 rows of Table 6, training on video segments of 160 frames enables seamless migration to video segments of any length without performance degradation. However, performance degradation occurs when the test length is reduced to 1 second (the second row), likely due to its duration being shorter than that of a single heartbeat. From the results at various lengths of testing, it is evident that RhythmMamba has truly learned the periodic patterns of rPPG. Moreover, it can handle ultra-long video inputs by splitting them into arbitrarily sized short video segments for processing and subsequent concatenation.

Furthermore, we conducted training on video segments of different lengths. As indicated by the first row and the last four rows of Table 6, there is a significant performance degradation when the video segment length increases. This degradation may be attributed to the substantial reduction in the count of training data as the length of the video segments increases.

4.7 Computational Cost

We also reported the parameters and multiply-accumulates (MACs) for all implemented methods, calculated under a video input size of $160 \times 128 \times 128$ ($T \times H \times W$). The results are presented in Table 7. Our method achieves state-of-the-art performance with fewer parameters and MACs, showcasing the potential for efficient mobile-level rPPG applications.

4.8 Visualization

As shown in the left half of Figure 2, we visualize the spectrum of an example from MMPD. From top to bottom, these represent the averaging of spectra across all channels in the frequency domain feed-forward stage of the last block, the power spectrum density of the rPPG signal before bandpass filtering at the end, and the power

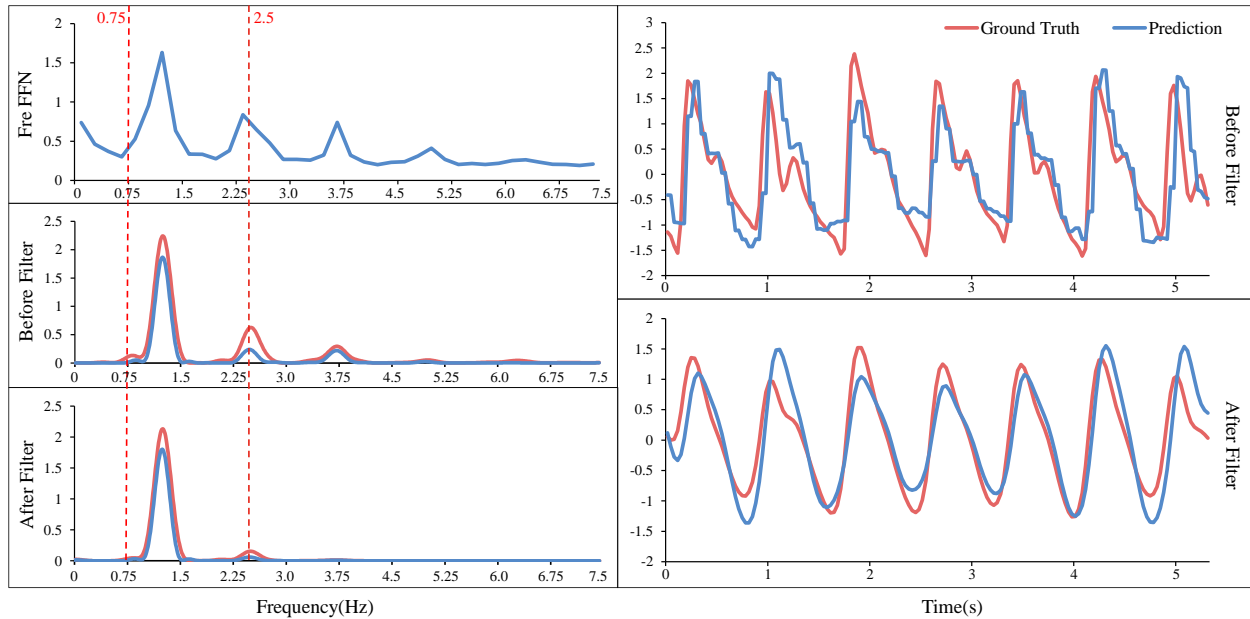


Figure 2: An example of results on MMPD.

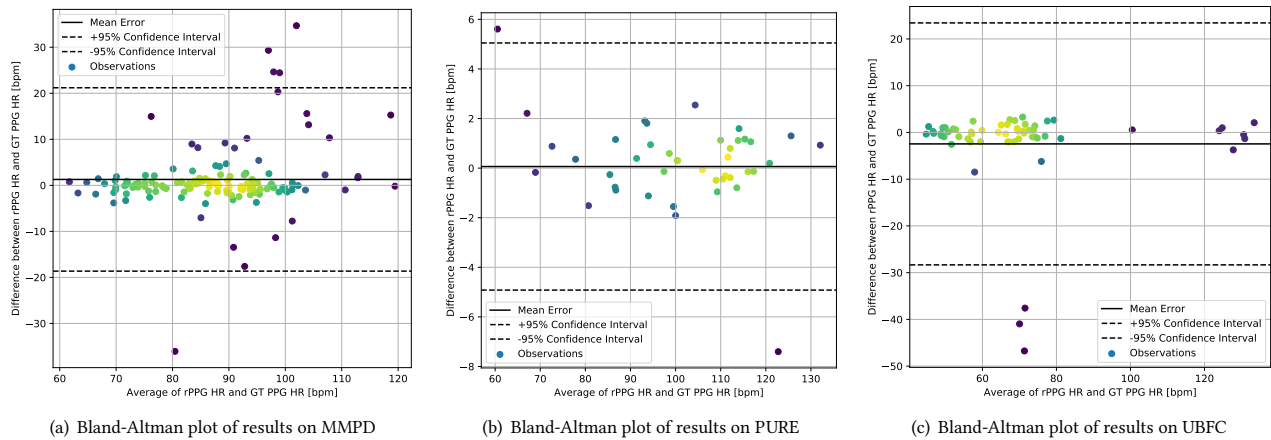


Figure 3: Bland-Altman plots of results.

spectrum density of rPPG after bandpass filtering. The range of 0.75-2.5Hz corresponds to the frequency band of heart rate. Due to the spectrum of Fre FFN being obtained through FFT, the number of frequency points in the spectrum depends on the input length, resulting in less smooth output. However, it still accurately captures the frequency domain characteristics of the BVP ground truth.

As shown in the right half of Figure 2, an example of the BVP waveform is provided to demonstrate the efficacy and precision of our approach. Notably, our model robustly captures the peaks and variations of PPG signals, serving as the core judgment basis for predicting heart rate from video data. Additionally, Bland-Altman plots of results are depicted, as shown in Figure 3, revealing a strong correlation between the prediction and ground truth.

5 CONCLUSION

Addressing the two core issues of rPPG, namely extracting weak rPPG signals from a large amount of spatiotemporal redundant video clips and understanding the periodic patterns of rPPG from long contexts, we propose RhythmMamba, which boasts strong long-range dependency modeling capabilities while maintaining linear complexity. It achieves state-of-the-art performance both within datasets and across datasets with reduced parameters and lower computational complexity. RhythmMamba can be applied to videos of arbitrary lengths after training and we envision it to serve as a new baseline for the rPPG community. Future explorations will focus on: 1. The generalization gap between RhythmMamba and real-world applications. 2. The feasibility of deployment on actual cameras.

REFERENCES

- [1] Anurag Arnab, Mostafa Dehghani, Georg Heigold, Chen Sun, Mario Lučić, and Cordelia Schmid. 2021. Vivit: A video vision transformer. In *Proceedings of the IEEE/CVF International Conference on Computer Vision*, 6836–6846.
- [2] Serge Bobbia, Richard Macwan, Yannick Benezeth, Alamin Mansouri, and Julien Dubois. 2019. Unsupervised skin tissue segmentation for remote photoplethysmography. *Pattern Recognition Letters* 124 (2019), 82–90.
- [3] Guo Chen, Yifei Huang, Jilan Xu, Baoqi Pei, Zhe Chen, Zhiqi Li, Jiahao Wang, Kunchang Li, Tong Lu, and Limin Wang. 2024. Video mamba suite: State space model as a versatile alternative for video understanding. *arXiv preprint arXiv:2403.09626* (2024).
- [4] Weixuan Chen and Daniel McDuff. 2018. Deepphys: Video-based physiological measurement using convolutional attention networks. In *Proceedings of the European Conference on Computer Vision (ECCV)*, 349–365.
- [5] Jae-Ho Choi, Ki-Bong Kang, and Kyung-Tae Kim. 2024. Fusion-Vital: Video-RF Fusion Transformer for Advanced Remote Physiological Measurement. In *Proceedings of the AAAI Conference on Artificial Intelligence*, Vol. 38, 1344–1352.
- [6] Joaquim Comas, Adria Ruiz, and Federico Sukno. 2022. Efficient remote photoplethysmography with temporal derivative modules and time-shift invariant loss. In *Proceedings of the IEEE/CVF Conference on Computer Vision and Pattern Recognition Workshops*, 2182–2191.
- [7] Rui Dai, Srijan Das, Kumara Kahatapitiya, Michael S Ryoo, and François Brémond. 2022. MS-TCT: multi-scale temporal convtransformer for action detection. In *Proceedings of the IEEE/CVF Conference on Computer Vision and Pattern Recognition*, 20041–20051.
- [8] Gerard De Haan and Vincent Jeanne. 2013. Robust pulse rate from chrominance-based rPPG. *IEEE Transactions on Biomedical Engineering* 60, 10 (2013), 2878–2886.
- [9] Gerard De Haan and Arno Van Leest. 2014. Improved motion robustness of remote-PPG by using the blood volume pulse signature. *Physiological measurement* 35, 9 (2014), 1913.
- [10] Alexey Dosovitskiy, Lucas Beyer, Alexander Kolesnikov, Dirk Weissenborn, Xi-aohua Zhai, Thomas Unterthiner, Mostafa Dehghani, Matthias Minderer, Georg Heigold, Sylvain Gelly, et al. 2020. An image is worth 16x16 words: Transformers for image recognition at scale. *arXiv preprint arXiv:2010.11929* (2020).
- [11] Jingda Du, Si-Qi Liu, Bochao Zhang, and Pong C Yuen. 2023. Dual-Bridging With Adversarial Noise Generation for Domain Adaptive rPPG Estimation. In *Proceedings of the IEEE/CVF Conference on Computer Vision and Pattern Recognition*, 10355–10364.
- [12] Daniel Y. Fu, Tri Dao, Khaled Kamal Saab, Armin W. Thomas, Atri Rudra, and Christopher Ré. 2023. Hungry Hungry Hippos: Towards Language Modeling with State Space Models. In *The Eleventh International Conference on Learning Representations, ICLR 2023, Kigali, Rwanda, May 1-5, 2023*. OpenReview.net. <https://openreview.net/pdf?id=COZDy0WYGg>
- [13] Albert Gu and Tri Dao. 2023. Mamba: Linear-time sequence modeling with selective state spaces. *arXiv preprint arXiv:2312.00752* (2023).
- [14] Albert Gu, Karan Goel, and Christopher Ré. 2022. Efficiently Modeling Long Sequences with Structured State Spaces. In *The Tenth International Conference on Learning Representations, ICLR 2022, Virtual Event, April 25-29, 2022*. OpenReview.net. <https://openreview.net/forum?id=uYLFoz1vIAC>
- [15] Anup Kumar Gupta, Rupesh Kumar, Lokendra Birla, and Puneet Gupta. 2023. RADIANT: Better rPPG estimation using signal embeddings and Transformer. In *Proceedings of the IEEE/CVF Winter Conference on Applications of Computer Vision*, 4976–4986.
- [16] Huazhang Hu, Sixun Dong, Yiqun Zhao, Dongze Lian, Zhengxin Li, and Shenghua Gao. 2022. Transrac: Encoding multi-scale temporal correlation with transformers for repetitive action counting. In *Proceedings of the IEEE/CVF Conference on Computer Vision and Pattern Recognition*, 19013–19022.
- [17] Bin Huang, Shen Hu, Zimeng Liu, Chun-Liang Lin, Junfeng Su, Changchen Zhao, Li Wang, and Wenjin Wang. 2023. Challenges and prospects of visual contactless physiological monitoring in clinical study. *NPJ Digital Medicine* 6, 1 (2023), 231.
- [18] Jiaqi Kang, Su Yang, and Weishan Zhang. 2022. Transppg: Two-stream transformer for remote heart rate estimate. *arXiv preprint arXiv:2201.10873* (2022).
- [19] Jun Kong, Yuhang Bian, and Min Jiang. 2022. MTT: Multi-scale temporal transformer for skeleton-based action recognition. *IEEE Signal Processing Letters* 29 (2022), 528–532.
- [20] Eugene Lee, Evan Chen, and Chen-Yi Lee. 2020. Meta-rppg: Remote heart rate estimation using a transductive meta-learner. In *Computer Vision–ECCV 2020: 16th European Conference, Glasgow, UK, August 23–28, 2020, Proceedings, Part XXVII* 16. Springer, 392–409.
- [21] Jun Seong Lee, Gytuae Hwang, Moonwook Ryu, and Sang Jun Lee. 2023. LSTC-rPPG: Long Short-Term Convolutional Network for Remote Photoplethysmography. In *Proceedings of the IEEE/CVF Conference on Computer Vision and Pattern Recognition Workshops*, 6014–6022.
- [22] Magdalena Lewandowska, Jacek Rumiński, Tomasz Kocejko, and Jędrzej Nowak. 2011. Measuring pulse rate with a webcam—a non-contact method for evaluating cardiac activity. In *2011 Federated Conference on Computer Science and Information Systems (FedCSIS)*. IEEE, 405–410.
- [23] Jianwei Li, Zitong Yu, and Jingang Shi. 2023. Learning motion-robust remote photoplethysmography through arbitrary resolution videos. In *Proceedings of the AAAI Conference on Artificial Intelligence*, Vol. 37, 1334–1342.
- [24] Kunchang Li, Xinhao Li, Yi Wang, Yanan He, Yali Wang, Limin Wang, and Yu Qiao. 2024. Videomamba: State space model for efficient video understanding. *arXiv preprint arXiv:2403.06977* (2024).
- [25] Xiaobai Li, Jie Chen, Guoying Zhao, and Matti Pietikainen. 2014. Remote heart rate measurement from face videos under realistic situations. In *Proceedings of the IEEE Conference on Computer Vision and Pattern Recognition*, 4264–4271.
- [26] Mingxuan Liu, Jiankai Tang, Haoxiang Li, Jiahao Qi, Siwei Li, Kegang Wang, Yuntao Wang, and Hong Chen. 2024. Spiking-PhysFormer: Camera-Based Remote Photoplethysmography with Parallel Spike-driven Transformer. *arXiv:2402.04798* [cs.CV]
- [27] Xin Liu, Josh Fromm, Shwetak Patel, and Daniel McDuff. 2020. Multi-task temporal shift attention networks for on-device contactless vitals measurement. *Advances in Neural Information Processing Systems* 33 (2020), 19400–19411.
- [28] Xin Liu, Brian Hill, Ziheng Jiang, Shwetak Patel, and Daniel McDuff. 2023. Efficientphys: Enabling simple, fast and accurate camera-based cardiac measurement. In *Proceedings of the IEEE/CVF Winter Conference on Applications of Computer Vision*, 5008–5017.
- [29] Xin Liu, Girish Narayanswamy, Akshay Paruchuri, Xiaoyu Zhang, Jiankai Tang, Yuzhe Zhang, Soumyadip Sengupta, Shwetak Patel, Yuntao Wang, and Daniel McDuff. 2023. rPPG-Toolbox: Deep Remote PPG Toolbox. In *Thirty-seventh Conference on Neural Information Processing Systems Datasets and Benchmarks Track*. <https://openreview.net/forum?id=q4XNX15kSe>
- [30] Yue Liu, Yunjie Tian, Yuzhong Zhao, Hongtian Yu, Lingxi Xie, Yaowei Wang, Qixiang Ye, and Yunfan Liu. 2024. Vmamba: Visual state space model. *arXiv preprint arXiv:2401.10166* (2024).
- [31] Birla Lokendra and Gupta Puneet. 2022. AND-rPPG: A novel denoising-rPPG network for improving remote heart rate estimation. *Computers in biology and medicine* 141 (2022), 105146.
- [32] Hao Lu, Hu Han, and S Kevin Zhou. 2021. Dual-gan: Joint bvp and noise modeling for remote physiological measurement. In *Proceedings of the IEEE/CVF Conference on Computer Vision and Pattern Recognition*, 12404–12413.
- [33] Hao Lu, Zitong Yu, Xuesong Niu, and Ying-Cong Chen. 2023. Neuron Structure Modeling for Generalizable Remote Physiological Measurement. In *Proceedings of the IEEE/CVF Conference on Computer Vision and Pattern Recognition*, 18589–18599.
- [34] Daniel McDuff. 2023. Camera measurement of physiological vital signs. *Comput. Surveys* 55, 9 (2023), 1–40.
- [35] Harsh Mehta, Ankit Gupta, Ashok Cutkosky, and Behnam Neyshabur. 2023. Long Range Language Modeling via Gated State Spaces. In *The Eleventh International Conference on Learning Representations, ICLR 2023, Kigali, Rwanda, May 1-5, 2023*. OpenReview.net. <https://openreview.net/pdf?id=5MkYIYCbva>
- [36] Xuesong Niu, Hu Han, Shiguang Shan, and Xilin Chen. 2018. Synrhythm: Learning a deep heart rate estimator from general to specific. In *2018 24th International Conference on Pattern Recognition (ICPR)*. IEEE, 3580–3585.
- [37] Xuesong Niu, Shiguang Shan, Hu Han, and Xilin Chen. 2019. Rhythmnet: End-to-end heart rate estimation from face via spatial-temporal representation. *IEEE Transactions on Image Processing* 29 (2019), 2409–2423.
- [38] Xuesong Niu, Zitong Yu, Hu Han, Xiaobai Li, Shiguang Shan, and Guoying Zhao. 2020. Video-based remote physiological measurement via cross-verified feature disentangling. In *Computer Vision–ECCV 2020: 16th European Conference, Glasgow, UK, August 23–28, 2020, Proceedings, Part II* 16. Springer, 295–310.
- [39] Badri N Patro and Vijay S Agneeswaran. 2024. SiMBA: Simplified Mamba-Based Architecture for Vision and Multivariate Time series. *arXiv preprint arXiv:2403.15360* (2024).
- [40] Christian S Pilz, Sebastian Zaunseder, Jarek Krajewski, and Vladimir Blazek. 2018. Local group invariance for heart rate estimation from face videos in the wild. In *Proceedings of the IEEE Conference on Computer Vision and Pattern Recognition Workshops*, 1254–1262.
- [41] Ming-Zher Poh, Daniel J McDuff, and Rosalind W Picard. 2010. Non-contact, automated cardiac pulse measurements using video imaging and blind source separation. *Optics express* 18, 10 (2010), 10762–10774.
- [42] Ambareesh Revanur, Ananyananda Dasari, Conrad S Tucker, and Laszlo A Jeni. 2022. Instantaneous physiological estimation using video transformers. In *Multimodal AI in healthcare: A paradigm shift in health intelligence*. Springer, 307–319.
- [43] Hang Shao, Lei Luo, Jianjun Qian, Shuo Chen, Chuanfei Hu, and Jian Yang. 2023. TranPhys: Spatiotemporal Masked Transformer Steered Remote Photoplethysmography Estimation. *IEEE Transactions on Circuits and Systems for Video Technology* (2023).
- [44] Jimmy T. H. Smith, Andrew Warrington, and Scott W. Linderman. 2023. Simplified State Space Layers for Sequence Modeling. In *The Eleventh International*

- Conference on Learning Representations, ICLR 2023, Kigali, Rwanda, May 1-5, 2023. OpenReview.net. <https://openreview.net/pdf?id=Ai8Hw3AXqks>
- [45] Rencheng Song, Huan Chen, Juan Cheng, Chang Li, Yu Liu, and Xun Chen. 2021. PulseGAN: Learning to generate realistic pulse waveforms in remote photoplethysmography. *IEEE Journal of Biomedical and Health Informatics* 25, 5 (2021), 1373–1384.
- [46] Radim Špetlík, Vojtech Franc, and Jirí Matas. 2018. Visual heart rate estimation with convolutional neural network. In *Proceedings of the British Machine Vision Conference, Newcastle, UK*, 3–6.
- [47] Ronny Stricker, Steffen Müller, and Horst-Michael Gross. 2014. Non-contact video-based pulse rate measurement on a mobile service robot. In *The 23rd IEEE International Symposium on Robot and Human Interactive Communication*. IEEE, 1056–1062.
- [48] Jiankai Tang, Kequan Chen, Yuntao Wang, Yuanchun Shi, Shwetak Patel, Daniel McDuff, and Xin Liu. 2023. MMPD: Multi-Domain Mobile Video Physiology Dataset. In *45th Annual International Conference of the IEEE Engineering in Medicine and Biology Society*.
- [49] Yun-Yun Tsou, Yi-An Lee, Chiou-Ting Hsu, and Shang-Hung Chang. 2020. Siamese-rPPG network: Remote photoplethysmography signal estimation from face videos. In *Proceedings of the 35th annual ACM symposium on applied computing*, 2066–2073.
- [50] Ashish Vaswani, Noam Shazeer, Niki Parmar, Jakob Uszkoreit, Llion Jones, Aidan N Gomez, Łukasz Kaiser, and Illia Polosukhin. 2017. Attention is all you need. *Advances in neural information processing systems* 30 (2017).
- [51] Wim Verkruyse, Lars O Svaasand, and J Stuart Nelson. 2008. Remote plethysmographic imaging using ambient light. *Optics express* 16, 26 (2008), 21434–21445.
- [52] Wenjin Wang, Albertus C Den Brinker, Sander Stuijk, and Gerard De Haan. 2016. Algorithmic principles of remote PPG. *IEEE Transactions on Biomedical Engineering* 64, 7 (2016), 1479–1491.
- [53] Wenjin Wang, Sander Stuijk, and Gerard De Haan. 2015. A novel algorithm for remote photoplethysmography: Spatial subspace rotation. *IEEE Transactions on Biomedical Engineering* 63, 9 (2015), 1974–1984.
- [54] Yijun Yang, Zhaohu Xing, and Lei Zhu. 2024. Vivim: a video vision mamba for medical video object segmentation. *arXiv preprint arXiv:2401.14168* (2024).
- [55] Kun Yi, Qi Zhang, Wei Fan, Shoujin Wang, Pengyang Wang, Hui He, Ning An, Defu Lian, Longbing Cao, and Zhendong Niu. 2024. Frequency-domain MLPs are more effective learners in time series forecasting. *Advances in Neural Information Processing Systems* 36 (2024).
- [56] Zitong Yu, Xiaobai Li, Xuesong Niu, Jingang Shi, and Guoying Zhao. 2020. Autohr: A strong end-to-end baseline for remote heart rate measurement with neural searching. *IEEE Signal Processing Letters* 27 (2020), 1245–1249.
- [57] Zitong Yu, Xiaobai Li, Pichao Wang, and Guoying Zhao. 2021. Transrppg: Remote photoplethysmography transformer for 3d mask face presentation attack detection. *IEEE Signal Processing Letters* 28 (2021), 1290–1294.
- [58] Zitong Yu, Xiaobai Li, and Guoying Zhao. 2019. Remote photoplethysmograph signal measurement from facial videos using spatio-temporal networks. In *30th British Machine Vision Conference: BMVC 2019, 9th-12th September 2019, Cardiff, UK. The British Machine Vision Conference (BMVC)*.
- [59] Zitong Yu, Wei Peng, Xiaobai Li, Xiaopeng Hong, and Guoying Zhao. 2019. Remote heart rate measurement from highly compressed facial videos: an end-to-end deep learning solution with video enhancement. In *Proceedings of the IEEE/CVF International Conference on Computer Vision*, 151–160.
- [60] Zitong Yu, Yuming Shen, Jingang Shi, Hengshuang Zhao, Yawen Cui, Jiehua Zhang, Philip Torr, and Guoying Zhao. 2023. Physformer++: Facial video-based physiological measurement with slowfast temporal difference transformer. *International Journal of Computer Vision* 131, 6 (2023), 1307–1330.
- [61] Zitong Yu, Yuming Shen, Jingang Shi, Hengshuang Zhao, Philip HS Torr, and Guoying Zhao. 2022. Physformer: Facial video-based physiological measurement with temporal difference transformer. In *Proceedings of the IEEE/CVF Conference on Computer Vision and Pattern Recognition*, 4186–4196.
- [62] Xiaobiao Zhang, Zhaoqiang Xia, Lili Liu, and Xiaoyi Feng. 2023. Demodulation based transformer for rppg generation and heart rate estimation. *IEEE Signal Processing Letters* (2023).
- [63] Yu Zhao, Bochao Zou, Fan Yang, Lin Lu, Abdelkader Nasreddine Belkacem, and Chao Chen. 2021. Video-based physiological measurement using 3d central difference convolution attention network. In *2021 IEEE International Joint Conference on Biometrics (IJCB)*. IEEE, 1–6.
- [64] Lianghui Zhu, Bencheng Liao, Qian Zhang, Xinlong Wang, Wenyu Liu, and Xinggang Wang. 2024. Vision mamba: Efficient visual representation learning with bidirectional state space model. *arXiv preprint arXiv:2401.09417* (2024).
- [65] Bochao Zou, Zizheng Guo, Jiansheng Chen, and Huimin Ma. 2024. RhythmFormer: Extracting rPPG Signals Based on Hierarchical Temporal Periodic Transformer. *arXiv preprint arXiv:2402.12788* (2024).